Journal Name

ARTICLE

A Thermal Energy Storage Prototype using Sodium Magnesium Hydride†

Received 00th January 20xx,
Accepted 00th January 20xx

DOI: 10.1039/x0xx00000x

www.rsc.org/

L. Poupin,[a] T. D. Humphries,[a]* M. Paskevicius[a] and C. E. Buckley[a]

Metal hydrides present favourable thermal storage properties particularly due to their high energy density during thermochemical hydrogenation. For this purpose, sodium magnesium hydride ($NaMgH_3$) has shown promising qualities that could lead to an industrialised application, but first requires to be examined on a lab-scale under realistic operating conditions. Herein, the cycling reversibility of $NaMgH_3$ is undertaken on a 150 g scale with active heat extraction and delivery using superheated water vapour as the heat transfer fluid. The thermal and cycling properties of the hydride material are enhanced by addition of TiB_2 and exfoliated natural graphite. Over 40 cycles the $NaMgH_3$ showed minimal loss in capacity, but revealed difficulties in terms of thermal management to avoid local overheating, resulting in the production of undesired molten sodium metal. The temperature cycling showed a hydrogen flow culminating at 1 g/h, which was insufficient to ensure thermal energy retrieval. The increase of the inlet hydrogen pressure has been shown to be instrumental in achieving an acceptable flow rate of 10 g/h. Indeed, this design, despite high heat losses to the environment, was able to supply a third of the chemical energy available to the heat transfer fluid.

Introduction

Modern society and technological development is leading us to an increasing energy dependence, meanwhile conventional fossil fuels are being depleted at an alarming rate while also triggering severe changes in our biosphere.[1] Developing sustainable energy solutions is now urgent. Solar power is a reliable energy source and efficient capture systems are well developed. However, their deployment for base-load power is hindered by the requirement of an energy storage system. Solar thermal power is amongst the most promising high capacity power plant technology, but high temperature thermal storage technology is still a major technical issue to overcome.[2] The majority of high temperature thermal solar power plants use molten nitrate salts as a sensible heat (specific heat) storage medium.[3] However, the decomposition temperature of Na/K nitrate above 565 °C hinders its maximum operation temperature.[4] Moreover, the thermal energy density of ≈ 100 Wh/kg must be increased to improve efficiency and decrease costs.[5] Several researchers have devoted their efforts into developing systems with higher energy densities, for example via thermochemical energy storage. More specifically, hydrogen sorption in metal hydrides has been reported to offer a potential increase by up to a factor of 55 as opposed to sensible heat storage.[6,7]

Metal hydrides have been investigated as thermal energy storage (TES) materials since the 1970's.[8] This interest was triggered by studies on MgH_2, which offers a theoretical hydrogen capacity of 7.7 wt% H, and high operating temperatures of ~300 °C are required due to the enthalpy of reaction of ΔH_{des} = 74.1 kJ/mol H_2.[9] During the past decade, metal hydrides as TES materials have been investigated intensively.[3,10-16] Due to their relatively high hydrogen capacities, high enthalpy of reaction and low cost; three metals (magnesium, sodium and calcium) seem to be eligible for long term, high temperature energy storage. But each type of system presents technical challenges that must be overcome to be a successful and commercially viable TES system.

Calcium hydride is known for having a high energy density of 171 kJ/mol of H_2.[17] This in turn leads to a high temperature of hydrogenation which occurs at 1050 °C under 1 bar H_2, therefore providing a possible TES solution for high efficiency solar power technologies such as Stirling dishes.[18] Further investigation is required to fully understand the material properties and develop a reliable containment material for high temperature storage near 850 °C. Magnesium hydride offers a reliable and consistent hydrogen storage capacity during hydrogen cycling when catalysed. The addition of additives (e.g. TiB_2) can improve sorption kinetics and cycling performance by acting as a particle refinement agent which controls the MgH_2 particle size and prevents sintering.[19, 20]

Sodium based hydrides are capable of absorbing and desorbing hydrogen over a wide temperature range. [21,22] Sodium alanate ($NaAlH_4$) has a theoretical cycling temperature range between 31 and 181°C for a pressure range of 1 and 150 bar H_2, while sodium magnesium hydride fluoride ($NaMgH_2F$) cycles up to

[a] Department of Physics and Astronomy, Fuels and Energy Technology Institute, Curtin University, GPO Box U1987, Perth, WA 6845, Australia.
*E-mail: terry_humphries81@hotmail.com
†Electronic Supplementary Information (ESI) available: XRD data, Van't Hoff plot, PCI data, DSC data and Kissinger plot. See DOI:10.1039/x0xx0000x

500 °C and 6 bar but quickly loses 70% of its cycling capacity.[21] The perovskite, sodium magnesium hydride, has received interest due to its flat equilibrium hydrogen desorption plateau and practically negligible hysteresis. Bouamrane *et al.* first determined its standard enthalpy of formation to be $\Delta H_f = -231$ kJ/mol,[22,23] whilst Ikeda *et al.* reported successful hydrogen reversibility of the material and identified a two-step reaction pathway that releases 6.0 wt% H_2 by pressure composition isotherm (PCI) analysis (eqs 1-2).[24] Sheppard *et al.* further examined the decomposition thermodynamics, calculating the enthalpy and entropy for the two steps to be ΔH = 86.6 kJ/mol H_2 with ΔS = 132.2 J/mol H_2.K and ΔH = 117 kJ/mol H_2.K with ΔS = 168 J/mol H_2.K, respectively.

$$NaMgH_3 \rightarrow NaH + Mg + H_2 \quad (1)$$

$$NaH \rightarrow Na(l) + 0.5H_2 \quad (2)$$

Sheppard *et al.* also addressed the reversible desorption and absorption of hydrogen from $NaMgH_3$, which demonstrates negligible hysteresis for the reaction's first step (eqn. 1).[25] It was also noted that the second desorption step (eqn. 2) leads to a macroscopic segregation of metallic Na and Mg, inducing a loss of hydrogen capacity over cycling, therefore only the first decomposition step should be considered for long term application.

Recently, concentrated efforts to improve the sorption kinetics of $NaMgH_3$ have been undertaken. S.Tao *et al.* replaced 10 wt% of the sodium in $NaMgH_3$ with potassium and in the process lowered the activation energy of the first step from 180.2 kJ/mol to 141.3 kJ/mol.[26] This modification also lowered the onset of decomposition temperature by approximately 50 °C and increased the desorption kinetics by a factor of two at 365 °C. Wang *et al.* doped $NaMgH_3$ with K_2TiF_6 (0.042 wt%) and reduced the activation energy to 153.35 kJ/mol,[27] allowing desorption of 90% of the hydrogen capacity in 20 min at 365 °C, compared to only 60% for the pristine material in the same timeframe. The addition of 2.5 wt% carbon nanotubes or graphene oxide by ball milling also reduces the activation energy of the first step to 113.8 kJ/mol, while also allowing 90% dehydrogenation in 20 min at 365 °C.[28]

For a material to be eligible for thermal storage applications, the material must be chemically reversible without continuous losses of hydrogen capacity. On a laboratory scale, it has been shown that $NaMgH_3$ could offer such reversibility, but only 10 cycles have been reported thus far.[29] Consequently, it seems vital to examine the feasibility of such material on a relevant scale that allows extrapolation to solar thermal power plants. In addition to up scaling, testing must consider heat supply and extraction from the powder bed. Since the 1980's, a broad range of thermochemical reactor modelling studies have been reported. As underlined by Yang *et al.*[30] and Jiao *et al.*,[31] optimising a reactor scheme results in optimising its thermal management; that is why even low temperature reactor models are an important source of information for thermal energy storage. In that regard, the addition of metallic foam has shown interesting results[32] as have heat pipes[33] or running a heat transfer fluid (HTF) within the hydride bed.[34] Designs including a HTF for energy removal have been further studied, and showed that in the case of using a powdered hydride, an embedded coil is preferred over a bundle of straight tubes for efficient thermal energy exchange.[35] In the case of high temperature thermal storage thermal management becomes far more important due to the larger thermal gradients.[36, 37] The overall reactor's design/shape has to provide short heat diffusion pathways between any point of the hydride bed and the HTF channel,[38] and for this purpose, carbon based additives can offer significant improvements compared to the thermal conductivity of bulk materials with low thermal conductivities.[39-41] High temperature thermal energy storage in metal hydride tanks has previously been attempted. Paskevicius *et al.* reported a consistent cycling reversibility in 18 g of magnesium hydride pellets (with additives) in a 2.54 cm stainless steel tube with a pressurised water HTF pipe placed in the reactor's centre and a hydrogen gas feed at one end. They concluded that one major obstacle was the high level of environmental heat losses when operating at 350 °C, even with significant insulation. It was difficult to extract the heat from the energetic release of hydrogen absorption due to the small heat transfer area between hydride and HTF.[36] In 2016, Dong *et al.* scaled up and improved the MgH_2 reactor design by embedding a coil in the hydride powder bed and added a porous rod in the reactor centre to ensure an even hydrogen supply through the reactor's length and thus achieved more homogenous response of the reactor.[37] The convenient use of supercritical water as a heat exchanger was also shown in both of these studies. Urbanczyk *et al.* conducted a thermal storage reactor experiment using 211 g of Mg_2FeH_6 with operating temperatures of up to 550 °C and a H_2 pressure up to 77 bar.[42] Here, a bundle of stainless-steel tubes encased the hydride with molten salts as the HTF to ensure high thermal exchange. Again, this study encountered difficulties with thermal management due to a high level of heat losses. In addition, some magnesium sintering issues were recorded, likely to be caused by the high working temperature.

In the present study, the thermochemical cycling reversibility of sodium magnesium hydride is demonstrated with the addition of 2 mol% TiB_2 as a particle refinement and anti-sintering agent. The thermodynamics and kinetics properties, as well as operational working limits are also studied in detail on a gram scale. Secondly, a 150 g scale reactor prototype containing $NaMgH_3$ was designed and tested under realistic operating conditions. This design aims to improve thermal management of the system and determine thermal energy transfer between the metal hydride bed and heat transfer fluid.

Experimental

Material preparation

Metal hydrides are sensitive to moisture and oxygen, therefore, all manipulation of chemicals were performed inside an argon filled glovebox, in which H_2O/O_2 levels were typically kept below 1 ppm. $NaMgH_3$ was synthesised from an equimolar mixture of NaH (Sigma-Aldrich, 95%), MgH_2 or Mg (Sigma-Aldrich, 98%). MgH_2 was synthesised within the laboratory by hydrogenating Mg powder at 400°C under 30 bar H_2 for 18 h. The partially

hydrogenated Mg was then ball milled (BM) for 3 hours with a ball-to-powder mass ratio of 10 : 1 in a Shaker Mill (Turbula T2C shaker-mixer) and annealed once again under identical conditions (400°C, 30 bar H_2, 18h). Synthesis of $NaMgH_3$ was achieved by first ball milling reagents (NaH and Mg/MgH_2) using stainless steel vials (150 ml in volume) and balls (equal numbers of 1 g and 0.6 g stainless steel balls). The ball to powder ratio was ~ 30:1 and the process was performed under argon for 240 min. The powder composite for the reactor was formed from an equimolar mixture of NaH and Mg with 2 mol% titanium boride (TiB_2, Sigma-Aldrich, <10 μm) and 20 wt% ENG (2.5–10 μm, SGL carbon). The ENG was previously outgassed for 12 h at 500 °C under dynamic vacuum, prior to the ball milling step. $NaMgH_3$ formation was observed after annealing the reactants at 380 °C under a minimum pressure of 20 bar H_2 for 6 hours.

Material characterisation

Quantitative phase analysis of the ball-milled and annealed mixtures was performed by powder X-ray diffractometry (XRD, Bruker D8 advance, λ = 1.5418 Å). Samples were loaded into a sample holder made of polymethylmethacrylate (PMMA), a hemispherical cap ensured that oxidation of the sample did not occur during data acquisition. A broad hump in the XRD pattern was observed at 2Θ ~ 20° due to the PMMA, therefore data acquisition was started at 2Θ = 20°. TOPAS (Bruker) software was used for XRD analysis using the Rietveld method to provide a quantitative calculation of the crystalline phases present, therefore validating materials synthesis.

Gram-scale hydrogen sorption and cycling investigations were conducted using a custom-made computer controlled Sieverts apparatus.[43] The sample holder (stainless steel 316) and reference volumes were calibrated at 25 °C and 450 °C, and a hydrogen diffusion factor through the stainless steel sample holder was implemented to provide a time and temperature dependent correction to hydrogen pressure measurements. The sample temperature acquisition was ensured by a K-type thermocouple calibrated by the manufacturer; a pressure transducer (Rosemount 3051S) with an accuracy of 14 mbar and a 4-wire platinum resistance temperature detector (for room temperature acquisition) were used for data acquisition. Pressure-composition Isotherm curves were processed through Igor Pro using a dedicated commercially developed software (Hyanalysis, Setaram). Thermogravimetric analysis (TGA) and differential Scanning Calorimetry (DSC) were simultaneously studied using a Mettler Toledo TGA/DSC. Samples were loaded in alumina crucibles (150 μL) with a weight of approximately 10 mg and heated from room temperature to 500 °C with a heating rate varying from 1 °C/min to 20 °C/min under argon flow (20 mL/min). Weight measurements have a ±20 µg accuracy and temperature uncertainty of ± 0.2 °C.

Reactor design

A reactor containing 150 g of reactor mix (RM, NaH/Mg/0.02TiB_2/ 20 wt% ENG) was designed and constructed. This is a third generation design incorporating the iterative findings from previous studies on metal hydride based CSP prototypes.[36, 37] The presented reactor consisted of two stainless steel tubes and corresponding Swagelok tube fittings, 40 cm length with 2.54 cm outer diameter and a wall thickness of 0.24 cm, mounted vertically in parallel. These reactors were placed directly adjacent to one another and were encapsulated in six ceramic bricks (from Bellis, conductivity of 0.65 W/m, thickness of 5 cm) with approximately 5 cm of an additional layer of aluminosilicate wool (Insulfrax LTX blanket, 0.1 W/m.K). A 0.6 cm diameter stainless steel porous rod (pore size = 1 µm, SIKA-R IS, GKN Sinter Metals Filters GmbH) was placed in the centre of each reactor to dissipate hydrogen gas throughout the

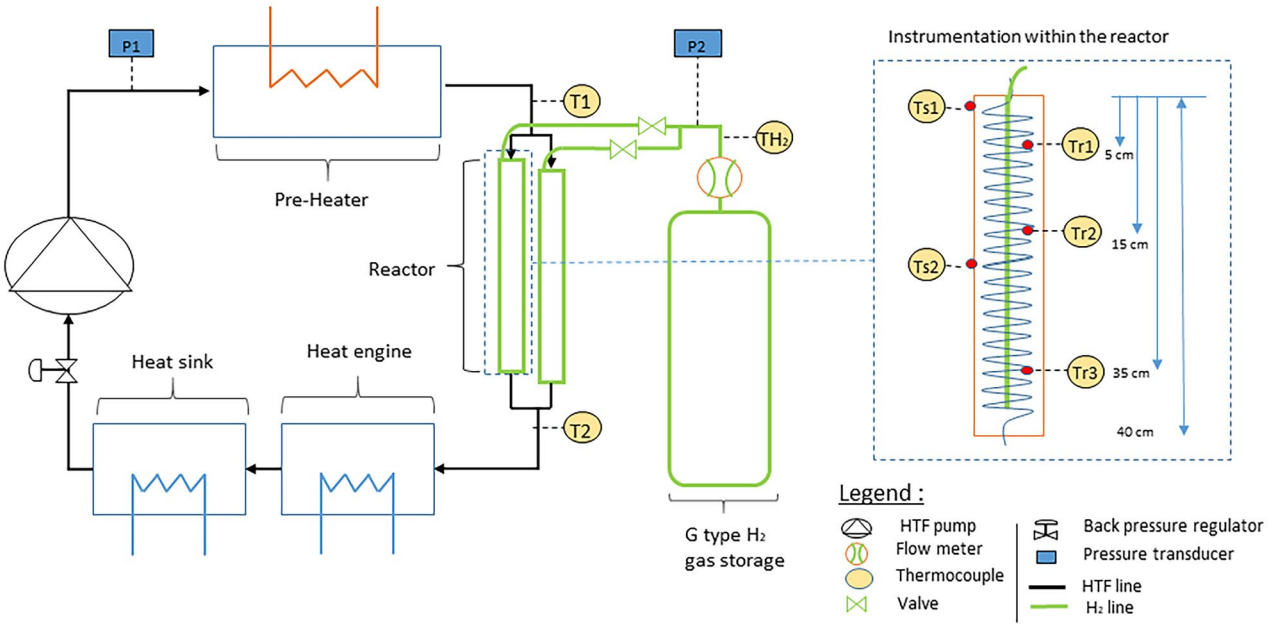

Figure 1. Schematic of the overall system with a detailed view of inside reactor. HTF, hydrogen, powder and reactor's envelope temperatures are respectively noted *T*, TH_2, *Tr* and *Ts*.

Journal Name

ARTICLE

entire tube length. Both tubes are then connected through a gas manifold (Swagelok) to a 50 L hydrogen bottle (G size) that ensured sufficient gas volume for absorption and desorption to minimise the operating pressure window. Since an embedded coil heat exchanger was elected as the most efficient design through modelling by Sekhar,[44] a 90 cm length of stainless steel coiled through the powder bed in each reactor. The coil diameter was equal to the reactor's radius to optimise thermal diffusion pathways between powder and coil. While filling the reactor, the reactor mix was poured and manually compacted inside the reactor.

The heat transfer fluid (HTF) within the coil was deionised water, pressurised to 140 bar using a back pressure regulator. The HTF flow was provided by a Gilson 305 piston pump with a flow rate of 8 ml/min. This flow rate, in tandem with the highest temperature achievable by the preheater allowed the HTF temperature to increase to ~500 °C before it entered the reactor. At these temperatures and pressure, the HTF is superheated water vapour.

In order to counteract environmental heat losses, 5 m of heating tape (1500 W) were wrapped around the ceramic bricks to provide a "hot background" (HB) at constant power output, independent of the reactors' thermal behaviour. The HB lowers the thermal gradient to the environment (average temperature of the outer surface equal to 375 °C) thus mimicking a larger scale thermal storage system where thermal losses are less dominant due to lower surface/volume ratios. The axial temperature gradient down the reactor was measured by three thermocouples (K type, 0.2 mm diameter) inserted in the powder bed (Figure 1), while two K-type thermocouples were placed on the outer skin.

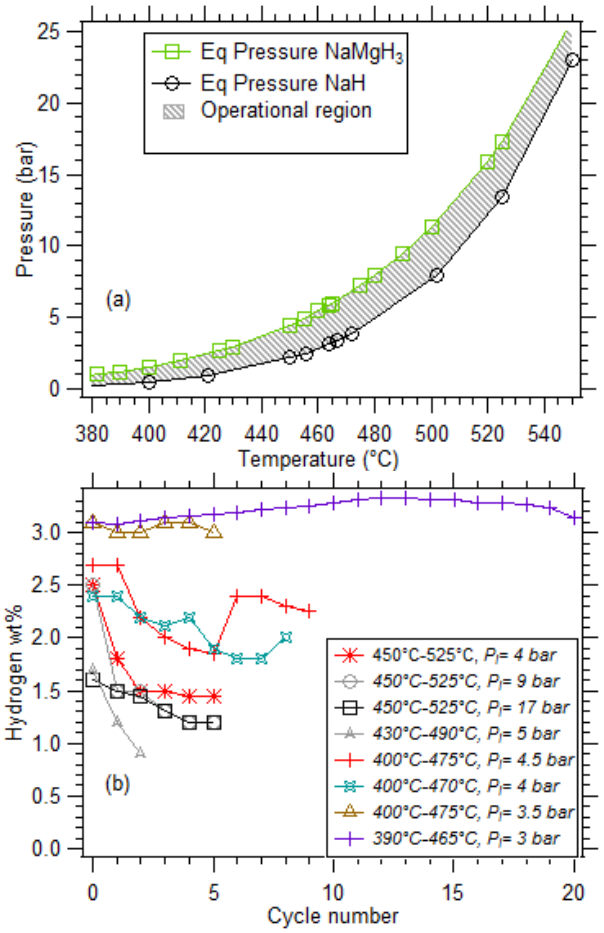

Figure 2. (a) Calculated Equilibrium pressure curves for $NaMgH_3$ → NaH + Mg + H_2 (square) and NaH → Na + H (circles).[21] (b) Hydrogen wt% desorbed during cycles using varied initial pressure (P_i) and cycling temperatures.

Result and discussion

Synthesis

Synthesis of $NaMgH_3$ from NaH and MgH_2 has been demonstrated in various manners including cryo-milling followed by annealing under hydrogen,[20] and ball-milling followed by annealing,[23] as well as reactive ball milling under hydrogen pressure.[9,45] However, the direct production of $NaMgH_3$ from NaH and Mg metal has not been reported. Thus, a comparison between using Mg or MgH_2 as a starting reagent was made. In both cases, 2 mol% TiB_2 was also added as a particle refinement agent due to Pitt et al.'s demonstration on its ability to improve kinetics.[20] NaH and Mg (or MgH_2) were milled with TiB_2 and annealed at 380 °C and 20 bar of H_2 for 6 h. XRD patterns of $NaMgH_3$ synthesised using various methods are shown in Figure S1 (†ESI). When NaH and MgH_2 are used as precursors, Rietveld analysis shows a 90 % yield of $NaMgH_3$, with minor remnants of starting reagents. If Mg is substituted for MgH_2, an 80 % yield is achieved. Hand-grinding the precursors, rather than ball milling, only yields 8 % $NaMgH_3$. The simplicity offered by the use of pure magnesium powder rather than magnesium hydride and the minimum change observed on the synthesis result justifies the choices of pure Mg for the following synthesis of a $NaMgH_3$ mixture.

Hydrogen cycling

Due to the irreversible hydrogen cycling of NaH, only the first dehydrogenation step for $NaMgH_3$ (eq. 1) is practically reversible. Therefore, an initial investigation was performed to establish the ideal operational temperature and pressure range. Ideally, the initial temperature and pressure needs to be optimised so that the system pressure will never fall below the

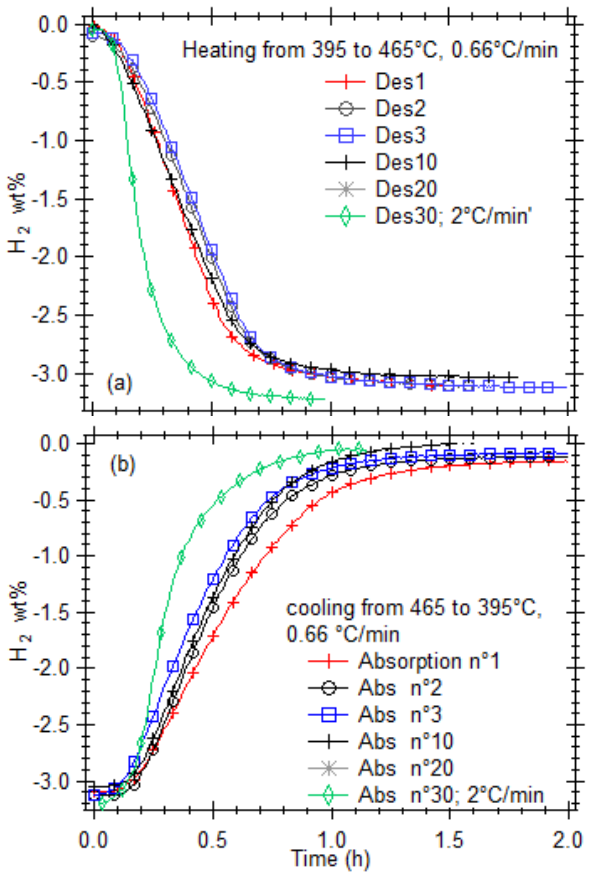

Figure 3. (a) Desorption and (b) Absorption kinetics of $NaMgH_3$ + 0.02TiB_2 over 30 cycles. Heating rate is 0.66 °C/min apart from cycle n°30 for at which the rate was increased to 2°C/min. Initial pressure for first desorption 3 bar.

equilibrium pressure of NaH during desorption, but will still be low enough to allow decomposition of $NaMgH_3$.

When the hydride is fully desorbed the system pressure (for a given temperature) has to reach a value within the narrow operational pressure range as shown in Figure 2(a) between the equilibrium pressures of $NaMgH_3$ and NaH.[21] The system gas volume is therefore chosen according to the sample's mass (hydrogen content) in order to avoid any decomposition of NaH. For these measurements, the system volume was 100 cm^3 for ~ 0.5 g of hydride. Figure 2(b) presents various hydrogen cycling attempts. Each of the cycles that operated between 450 and 525 °C led to a substantial decrease in the hydrogen capacity upon completion of the first cycle. It was only by reducing the temperature to below a maximum of 475 °C that a consistent amount of hydrogen was desorbed and reabsorbed. Apart from the sample cycled between 390 – 465 °C, some sodium metal was observed on the roof of the reactor after each of the other experiments, explaining the losses of hydrogen capacity. The presence of sodium metal suggests that either the system hydrogen pressure was not sufficient at some point during cycling, or localised temperature fluctuations caused the decomposition of NaH into Na (liquid/vapour).

More than 30 cycles were successfully completed using 0.5 g of $NaMgH_3$ with 2 mol% TiB_2, at temperatures between 400 and 465 °C and pressure varying between 3 and 6 bar. Figure 3

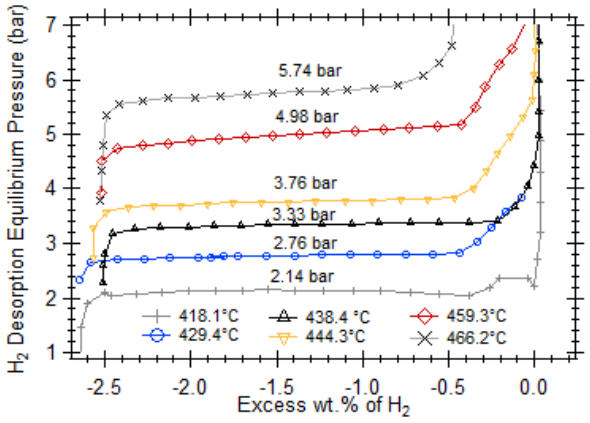

Figure 4. Pressure-composition-Isotherms (PCI) of the reactor mix between 418°C and 466°C.

illustrates the desorption and absorption kinetics during cycling. A consistent hydrogen capacity of approximately 3 wt% is observed during the entire experiment. For a heating and cooling time of 90 minutes (0.66 °C/min), 95% H_2 capacity is achieved within 1 hour. When the heating and cooling rate is increased to 2°C/min (30 min), 95% of hydrogen desorption is obtained in 30 min, whereas hydrogen absorption requires 45 min to reach 95% completion. Figure S2 (†ESI) shows the stability of the hydride after 30 cycles.

Thermodynamic and kinetic characterisation

The pressure-composition isotherms (PCI) of the reactor mix (RM = $NaMgH_3$, 0.02TiB_2, ENG (20 wt%)) are presented in Figure 4 over a temperature range of 418 to 466 °C. Each PCI curve was determined from the first step of $NaMgH_3$ decomposition (eq. 1). The hydrogen desorption plateau is relatively flat for the selected temperatures, occurring between 0.5 and 2.5 wt% H_2, with a total of 2.6 wt% H_2 capacity of the RM. Taking into account the additional 20 wt% of ENG, the measured 2.6 wt% H_2 measured is consistent with the reported value of 3.3 wt% H_2 for pure $NaMgH_3$.[25] A slight decrease in hydrogen capacity is observed for temperatures ≥ 444 °C. The desorption PCI plot for the 2 highest temperatures (459 and 466 °C) reveal a slope which is the beginning of a change in the desorption process. Figure S3 (†ESI) shows the absorption PCIs and reveals a negligible hysteresis phenomenon for temperatures below 444 °C, becoming significant (Δp = 0.5 bar) at 459.3 °C. Therefore, to avoid emergence of a hysteresis phenomenon, it is recommended not to operate $NaMgH_3$ at temperatures > 450 °C.

The thermodynamic values of ΔH = 86.4 ± 1.3 kJ/mol H_2 and ΔS = 131.4 ± 1.6 J/K/mol H_2 are determined via a Van't Hoff plot (Figure S4, †ESI). As shown in Table 1, they are deemed to be almost identical, within error, with those obtained previously by Sheppard et al.[21] This shows that the addition of the TiB_2 additive and ENG doesn't have a significant impact on the thermodynamics of hydrogen release from $NaMgH_3$.

A study of the activation energy (E_a) of decomposition for both $NaMgH_3$ and the RM ($NaMgH_3$, TiB_2, ENG) was undertaken by

Table 1. Enthalpy and entropy Comparison for hydrogen desorption

Enthalpy (kJ/mol H_2)	Entropy (J/mol H_2.K)	
86.6 ± 1	132.2 ± 1.3	Ref. [25]
92	123	Ref. [46]
94	140	Ref. [45]
88	116.2	Ref. [47]
86.4±1.3	131.4 ± 1.6	This work

DSC to understand if the additives impact the decomposition kinetics. The activation energy of pristine $NaMgH_3$ is found to be 160 ± 9.1 kJ/mol (Figure S5-S6, †ESI). The TiB_2 additive and/or ENG are inducing a lower activation energy determined to be 151.9 ± 6.6 kJ/mol. According to previous reports, Ti based alloys result in kinetic improvement, therefore lowering the activation energy. [20,45] However, it is also known that additives such as TiB_2 can act as anti-sintering agents,[20] where they may not directly impact kinetics, but prevent kinetic degradation over multiple cycles, and also may provide material stability at higher operating temperatures. Moreover, the addition of 20 wt% ENG was already shown to drastically increase the thermal conductivity of MgH_2 from 0.25 to 9 W/(m.K).[37, 40]

Lab-scale reactor: Temperature driven hydrogen desorption

After verifying the thermodynamic and kinetic properties and assessing the cyclability on a 1 g scale, the RM powder was loaded into the 150 g reactor. The design is described in the Experimental section and Figure 1. The 150 g lab-scale reactor was assessed through a series of different experiments to observe its response to different temperature and gas pressure conditions, which may mimic that of a full-scale CSP thermal storage system. Ideally, thermal energy storage for renewable electricity generation will stabilise and/or extend the heat energy supply to a heat engine or steam turbine during periods of insufficient renewable energy supply. For CSP, a metal hydride thermal storage should start generating heat (hydrogen absorption process) when the HTF drops to a selected temperature (for a constant HTF flow), therefore insuring a consistent amount of heat provided to the thermo-electric converter. Since the hydrogen sorption reaction is controlled by the hydride temperature, and its inherent equilibrium pressure at that temperature, it is possible to set the hydrogen gas pressure in the system to a value that initiates hydrogen absorption, and therefore heat generation, below a given temperature.

Firstly, hydrogen desorption from $NaMgH_3$ was initiated by setting the HTF temperature to 480 °C at a flow rate of 8 ml/min with an initial hydrogen pressure of 2.4 bar in the system. This step would account for a heat storage process. Note that the equilibrium pressure for $NaMgH_3$ at 480 °C is 7.3 bar,[21] inferring that the hydride will decompose at pressures below this pressure at 480 °C, given adequate kinetics. Figure 5(a) shows the system's thermal profile with the reactor skin (at the top of the reactor) reaching 450 °C after 6 h, whereas the hydride bed only reaches a maximum temperature of 435 °C. The hydride

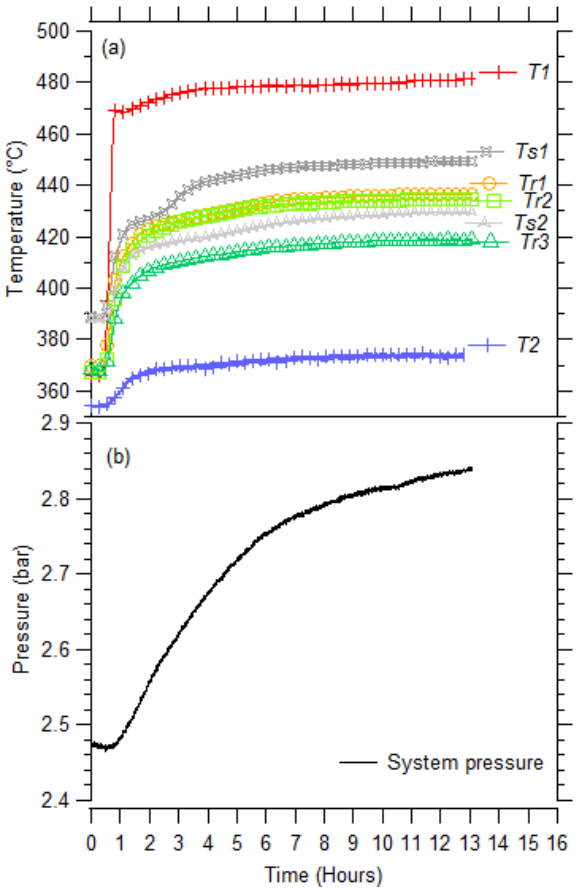

Figure 5. Temperature driven desorption inside the 150 g RM reactor. (a) Temperature profile within the reactor (*T1* and *T2*: inlet and outlet HTF, *Tr*: temperatures embedded in the reactor, *Ts*: Reactor skin temperature). (b) Pressure evolution during the reaction. Flow rate of HTF = 8mL/min.

bed itself has a vertical temperature gradient of 20 °C over its 30 cm length (between *Tr1* and *Tr3*, Figure 1).

A maximum system gas pressure of 2.84 bar H_2, Figure 5(b), is obtained after a 13 h desorption, equating to a hydrogen release of 1.2 wt.%, which is well below the expected 2.6 wt.%. The measured temperature inside the powder bed averages 428 °C, with environmental heat losses preventing higher temperatures to be reached. The theoretical temperature with an equilibrium pressure of 2.84 bar is 431 °C. This shows that hydrogen desorption continues until its equilibrium pressure, and further hydrogen release is hindered by the low average temperature of the hydride. Specifically, the measured temperature inside the powder bed ranges from 415 - 435 °C, resulting in a portion of the hydride being unable to reach the required temperature to further desorb hydrogen. This scenario introduces the likelihood that some hydride is active (hotter) and some inactive (cooler), and in this case the active hydride is approximately 65 g out of 150 g. The issue with low temperatures can be circumvented by increasing the reactor temperature or lowering the initial gas pressure, but the temperature gradient within the reactor bed causes difficulties. Generally, if the starting gas pressure is lowered then the second step (eq. 2) of the hydride decomposition (NaH → Na + $1/2H_2$) could occur in the hot regions of the reactor, which should be avoided because this step is irreversible. The NaH

Table 2. Optimisation of hydrogen desorption. HTF inlet temperature = 480°C, Flow rate = 8 mL/min.

Starting gas pressure (bar)	Final gas pressure (bar)	H_2 mass desorbed (g)	Corresponding active Reactor Mix mass (g)	Average Temperature (°C)	
				Hydride	Skin
2.43	2.7	1.08	41.5	421	430
2.46	2.85	1.58	60.0	428	436
2.47	2.81	1.4	53.9	423	432
2.01	2.47	1.99	76.7	418	440
1.99	2.54	2.2	84.9	430	440
1.54	2.08	2.2	84.5	420	445

equilibrium pressure at 450 °C is 2.16 bar.[48] This temperature was the highest measured on the reactor's skin so it is necessary to ensure a higher hydrogen gas pressure at this temperature. These complexities with a minor temperature gradient illustrate the difficulties in operating a large-scale reactor containing a metal hydride with a multi-step reaction pathway. In the case of $NaMgH_3$ it is even more challenging as its second step is technically irreversible.[21] To enable full hydrogen capacity/release, either the entire system must be isothermal or an alternative metal hydride should be utilised.

The hydrogen desorption from the lab-scale system was optimised by adjusting the initial and final pressures/temperatures along with thermal insulation adjustments. Lowering the starting system pressure would allow to trigger the desorption process at a lower temperature and a higher reactor temperature would higher the equilibrium pressure, thus extending the amount of hydrogen desorbed. Table 2 shows the various attempts to increase the amount of hydrogen desorbed and the corresponding active hydride mass. The different averaged temperatures were obtained by changing the hot background temperature settings and insulation thickness.

These optimisations (Table 2) show an effective gain on the quantity of released hydrogen by lowering the starting gas pressure in the system. For the same temperature conditions, a 2.46 bar starting pressure decreased to 1.99 bar offered a gain of approximately 25 g of active hydride mass. For the same pressure conditions (starting pressure of 2.4 bar), the temperature reactivity is such that a 6 - 7 °C gain on the hydride and skin temperature provides a 50 % increase in corresponding mass of active hydride. However, the temperature increase was inhibited to prevent the hydride powder from reaching 460 °C at any measurement point, which in turn prevented Na metal formation and excessive sintering. After optimisation of the system, it was feasible to desorb 57 % of the 2.6 wt% H_2 stored in the 150 g of reactor mix.

Lab-scale reactor: Temperature driven hydrogen absorption

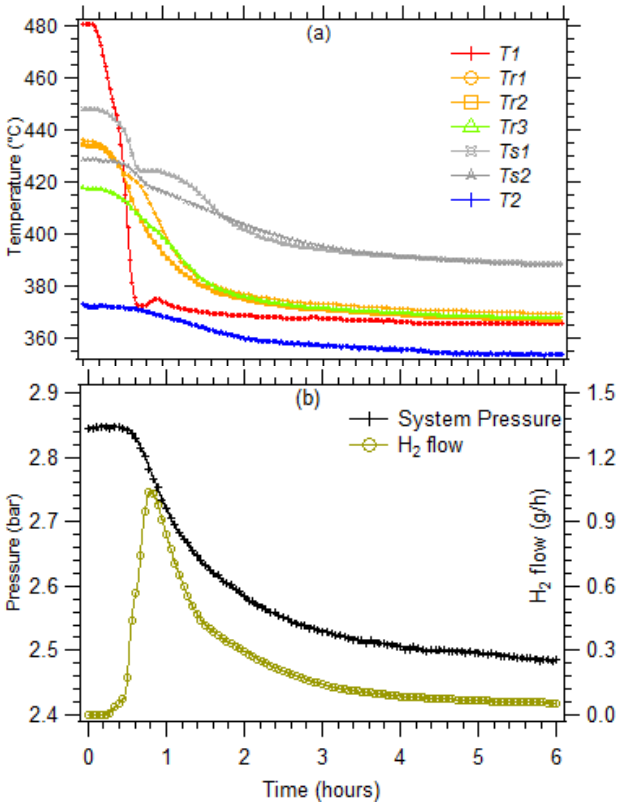

Figure 6. Temperature driven absorption for inlet HTF flowing at 8 ml/min dropping from T = 480°C to 380°C. (a) Temperature within the reactor. (b) System pressure and hydrogen flow.

As the hydrogen sorption cycles are driven by temperature and the corresponding hydrogen equilibrium pressure of $NaMgH_3$, the absorption process starts when the temperature drops, and hence the equilibrium pressure drops below the system gas pressure. To ensure full hydrogen absorption, the HTF inlet temperature is reduced from 480 to 380 °C (equilibrium pressure of 1 bar). This drop of the inlet temperature is replicating a need of heat discharge to the HTF, therefore a heat generating absorption of hydrogen. Figure 6 shows the reactor's temperature, hydrogen pressure and hydrogen flow from the volumetric gas store to the reactor during absorption, calculated from a differential pressure measurement via the equation (3):

$$q_m = \frac{C}{\sqrt{1-\beta^4}} \times \varepsilon \times \frac{\pi}{4} \times d^2 \times \sqrt{2\Delta p \times \rho} \qquad (3)$$

Where:

C: discharge coefficient (Reader-Harris Gallagher equation)

β(0.021): ratio between orifice and pipe diameter

ε: expansibility factor

d (0.01 cm): orifice diameter

Δp (Pa): instant differential pressure

ρ (kg/m³): instant volumetric mass

The different temperatures measured throughout the reactor during absorption are shown in Figure 6(a). The hydrogen absorption is exothermic, but a temperature rise is only observed in the top portion of the reactor skin (*Ts1*) and top portion of the metal hydride (*Tr1*). Figure 6(b) shows the gas

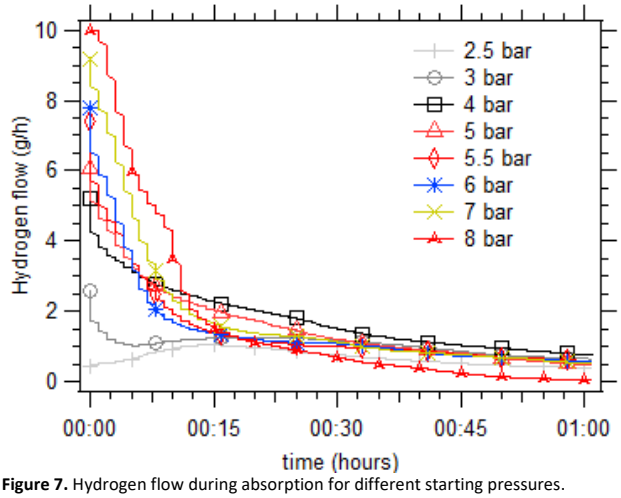

Figure 7. Hydrogen flow during absorption for different starting pressures.

pressure and hydrogen flow. The system's pressure stabilises after 6 hours, signifying the end of hydrogen absorption. The hydrogen flow reaches a maximum rate of 1 g/h, rapidly decreasing to lower than 0.2 g/h after a few hours. According to the quantity of hydrogen absorbed in this cycle (1.67 g), and the enthalpy of reaction (86.4 kJ/mol.H_2) then 71.2 kJ of heat was released from the reactor over 6 hours, equating an average of 3.3 W. This value is critically low, especially considering that the estimated radiative heat losses are approximately 10 W. If only the first hour of desorption is considered, with an average of 0.78 g H_2 absorbed, 9.3 W of heat is produced, which is not enough to increase the outlet HTF temperature. Therefore, it is necessary to increase the power generated by the hydride bed. As Bao et al. demonstrated, the absorption kinetics are one of the main parameters that drive the efficiency of a reactor.[49] Kinetics are mostly driven by intrinsic system parameters such as the hydride's hydrogen diffusivity, or thermal conductivity, however the most accessible leverage, in this study, is the differential pressure between the hydrogen gas pressure and the equilibrium pressure.

Lab-scale reactor: Absorption under an over pressure

In a real case scenario, the heat storage needs to provide a fast response to cover any lack of thermal energy that would diminish the electricity production. In that regard, thermal energy has to be generated and transmitted to the HTF rapidly, therefore to improve the reaction kinetics, the initial gas pressure used for hydrogen absorption was optimised. For each experiment, the hydrogen supply valve was opened when the HTF's temperature cooled to 400 °C.

Figure 7 illustrates the hydrogen flow measured during absorption with varying initial gas pressures in the system. Increasing the initial pressure allows for a significant improvement in reaction kinetics. More than six hours is required for absorption when driven solely by temperature (2.5 bar line), whereas one hour is required when an 8 bar H_2 pressure is also used. As such, at higher initial pressure, the hydrogen flow increased, in this case by a factor ten. The increased hydrogen uptake induced by a higher pressure is substantial during the first 20 min of the absorption process. It

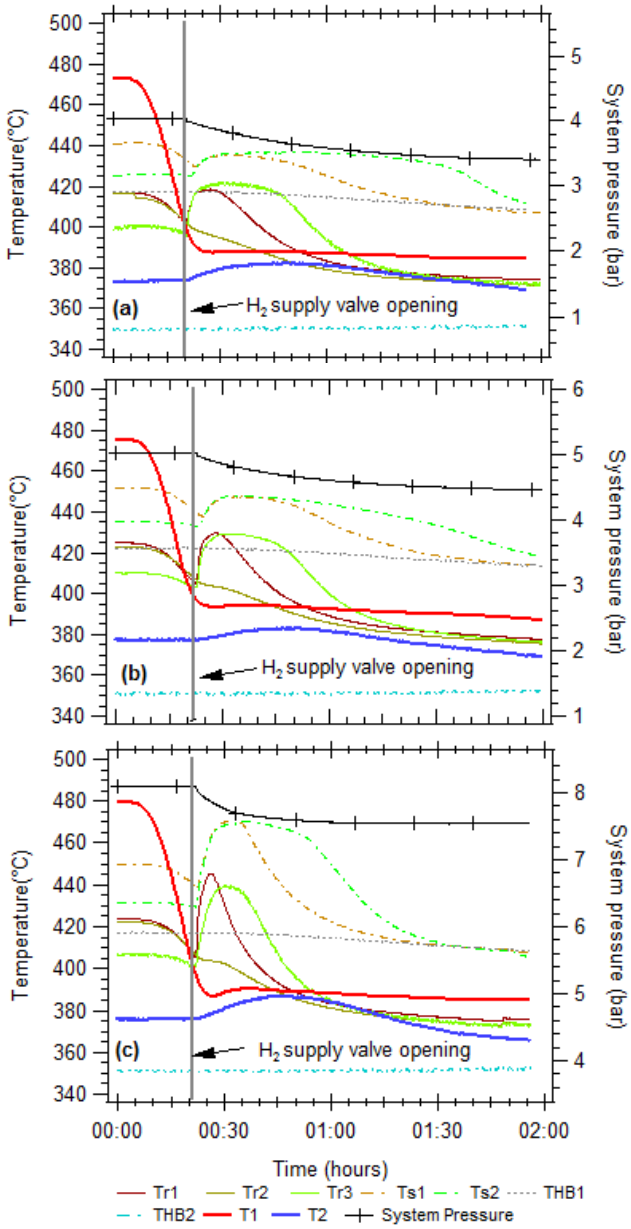

Figure 8. Temperature profile for the reactor at (a) 4 bar, (b) 5 bar and (c) 8 bar of initial hydrogen pressure. (*Tr1*, *Tr2*, *Tr3* : Inside reactor temperature ; *Ts1*, *Ts2* : reactor skin temperature ; *THB1*, *THB2* : Hot Background temperature ; *T1*: inlet HTF temperature, *T2*: outlet HTF temperature.

leads to a much larger thermal energy generation that increases the temperatures in the reactor (Figure 8). This figure shows the temperature raise in the reactor for the various thermocouple positions depicted in Figure 1. The data from thermocouple "*Tr2*" doesn't coincide with sensors *Tr1* or *Tr3* embedded in the powder. The reason proposed is that this sensor is in contact with the HTF coil, therefore displaying the HTF's temperature level. After hydrogen absorption initiates, both the hydride and the reactor surface show significant temperature increases (up to 40 °C) and remain at an elevated temperature for 30 to 60 min, respectively. The gradual thermal evolution shows that the hydride bed doesn't efficiently transfer generated heat to the HTF, illustrating the low effective thermal conductivity of the hydride bed. Despite the addition of ENG to increase thermal

Table 3. Time required for absorption and maximum hydrogen flow for varied initial hydrogen supply pressures.

Starting hydrogen pressure (bar)	1.5	3	4	5	5.5	6	7	8
Time (min)	378	238	167	150	148	128	115	68
Maximum hydrogen flow (g/h)	1.0	2.6	5.2	6.1	7.4	7.8	9.2	10.0

conductivity,[50] it seems that the augmentation is not effective, possibly due to the use of powder instead of compacts.

In all cases, after the initial temperature gain during absorption under elevated pressure, parts of the system (stainless steel and hydride powder) reach an isothermal state. The stainless steel reactor skin remains at a temperature 10 - 20°C higher than the powder bed. This could be explained by a greater thermal conductivity of the stainless steel and a greater hydrogen diffusion along the reactor walls hence a more homogenous reaction which releases greater quantities of energy.

One of the most important results for this experiment is that increasing the initial pressure, along with the consequential reduction of absorption time (shown in table 3) has resulted in a clear HTF outlet temperature rise. As much as a 10 °C increase is registered when an initial pressure of 8 bar hydrogen is applied. This result, given the water properties at 140 bar and 390 °C, is equal to 7.5 W of power extracted by the HTF.

To determine the distribution of thermal energy generated by the hydrogen absorption process, the system can be separated into 4 subsystems that are utilising the heat produced:

- The HTF, which represents heat extraction system providing energy for power production;
- The metal hydride, which is the heat source;
- The stainless steel reactor vessel;
- And the heat losses to the environment.

For each acquisition time step, the energy extracted by the HTF was calculated from the hydrogen mass flow, temperature difference between inlet and outlet and heat capacity at 390 °C. To account for the sensible thermal storage of the reactor, a reference experiment with identical thermal management was made with inhibited hydrogen sorption. The extracted energy associated with the hydrogen absorption is obtained by removing the reference experiment. The heat flow obtained was integrated over the time period for which the HTF outlet remains hotter than the reference (without hydrogenabsorption), and the overall energy extracted from the exothermic reaction was determined. The hydride's heat retention was determined by the average temperature increase of the hydride bed, the calculated hydride's active mass and its specific heat (3.9 kJ/kg.K). The latter is determined by summing up the specific heat at 425 °C provided by the NIST database[51] for $NaMgH_3$ and ENG. It was then integrated over the time period it remain hotter than the reference. The same procedure was used to access the energy accumulated within the stainless steel reactor vessel. With approximately 3 kg of steel, the

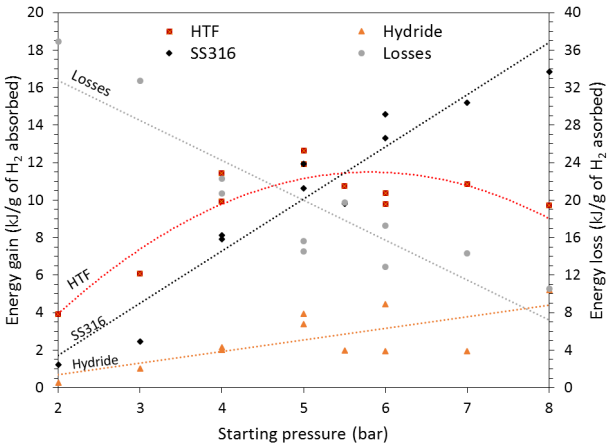

Figure 9. Thermal energy distribution after hydrogen absorption in the 4 subsystems for different hydrogen starting pressure. HTF, stainless steel reactor (SS136) and hydride curves gaining energy.

specific heat obtained from the NIST database[51] was determined to be 1938 J/K. The remaining losses are estimated by comparing the three previous energy quantities taken by the subsystems (HTF, metal hydride bed and reactor skin) to the theoretical energy available, considering the previously measured enthalpy of reaction.

Figure 9 presents the energy distribution for each of the four subsystems for a range of initial hydrogen gas pressures. It displays the heat energy per gram of hydrogen absorbed by the hydride to account for the slight variability of the hydrogen uptake in each cycle (2.2 - 2.7 g of H_2), which is due to minor temperature fluctuations during desorption cycles. The increase of the inlet pressure not only improves the kinetics but also diminishes heat losses, as the generated energy is dissipated through the other subsystems. A faster hydrogenation reaction allows energy to be distributed to the surrounding elements with a greater chance of being extracted by the HTF before being lost to the environment. Despite efforts to reduce the influence of environmental heat losses, this remains a prime energy consumer (25 - 80 %). The heat energy diverted to the stainless steel rises sharply at higher starting pressures (5 - 40 %). Ideally, a thermal storage reactor will have an optimised mass ratio between the containment material and hydride. 3 kg of stainless steel encases 150 g of hydride herein, which is not favourable, however this aspect shall be addressed in a real scale where the containment material is expected to be minimised to a small fraction (i.e. <5%) of the hydride mass. The contact area and/or its mass prevails over the HTF's heat extraction capacity. The hydride itself retains a smaller share of the produced energy, but still appears to withhold an increasing part of generated heat at higher starting pressures (10 - 30 %). The energy extracted by the HTF rises until reaching a maximum, which was for the experiment conducted at an initial hydrogen pressure of 5 bar. At this point, nearly 30 % of the energy generated is retrieved by the HTF, another 28 % and 9 % are absorbed by the steel and the hydride respectively, while more than a third is accounted for by heat losses. Above 5 bar of initial hydrogen pressure, the other subsystems (hydride, stainless steel) hold a greater part of the energy generated to

reach higher temperature levels, and eventually suffer increased thermal losses. This exposes the presence of an optimum hydrogen starting pressure for a given hydride, reactor design and heat extraction system. Consequently, further investigation is required to validate and understand the dependence of this phenomenon on system design.

Overall, the small scale of this experiment allows to prove the feasibility of thermal storage through metal hydride reactors, but also demonstrate the need of a larger scale to reduce the parasitic energy consumer effect. In addition, the cost of the raw materials is currently 5.8 €/kWh_{th} which is very similar to molten salts (5.25 €/kWh_{th}), while slightly higher than Mg_2FeH_6 (2.25 €/kWh_{th}). These costs will decrease upon large scale production. The relatively high cost of $NaMgH_3$ compared to Mg_2FeH_6 is due to the lower thermal energy density of $NaMgH_3$ (593 and 1352 kWh_{th}/m^3, respectively), although this is still twice as high as molten salts (222 kWh_{th}/m^3).[10]

Conclusions

This study illustrates many of the challenges and pitfalls that must be considered when designing a metal hydride based thermochemical heat storage system. $NaMgH_3$ is a particularly challenging metal hydride to use in a lab-scale prototype due to its multi-step decomposition and undesirable second step decomposition, which is technically irreversible. For the first time, $NaMgH_3$ synthesis was initiated from magnesium metal instead of MgH_2. Additives used to promote kinetics/cycling and thermal conductivity (TiB_2 and ENG) did not affect the thermodynamics of $NaMgH_3$, however, they did lower the activation energy of decomposition.

The lab-scale prototype was evaluated using 150 g of a hydride mixture coupled with dynamic thermal heat extraction and insertion using a high pressure steam HTF. More than 40 hydrogenation/dehydrogenation cycles were achieved to complete this study, showing a stable hydrogen capacity that was lower than expected due to the constraints of operating in a narrow temperature/pressure window to avoid decomposition of NaH. At a working pressure of 3 bar, as little as 30 °C separates the desired decomposition of $NaMgH_3$ and the undesired decomposition of NaH. This makes it important to minimise any thermal gradients in the system to ensure thermal homogeneity of the system, which can be challenging at small scale. The importance of the hydrogen supply pressure on the thermal energy retrieval was demonstrated, enabling an increase in the extracted energy by a factor 3, for a supply pressure of 5 bar instead of operating at the 2 bar equilibrium pressure for 420 °C. This result shows the need for a drastic improvement of reaction kinetics for a functional energy storage system. Unless a better catalyst is discovered, the integration of a hydrogen compressor into the thermal storage system, to guarantee an overpressure supply throughout operation cycles, is imperative. Moreover, the calculations of the quantity of energy consumed by the stainless steel reactor vessel itself and losses to the environment revealed their decisive impact on the overall system. It seems necessary to lower the ratio of the containment vessel mass to the metal hydride mass. Upscaling further is the primary way to overcome many of the issues discovered in this study.

Conflicts of interest

There are no conflicts to declare.

Acknowledgements

CEB and MP acknowledge the financial support of the Australian Research Council (ARC) for Linkage Project LP120101848, and CEB also acknowledges the ARC for funding LP150100730 and ARC LIEF grants LE0989180 and LE0775551, which enabled the XRD and gas sorption studies to be done. MP also acknowledges the ARC for Future Fellowship FT160100303. The authors acknowledge the facilities and technical assistance of the Microscopy & Microanalysis Facility of the John de Laeter Centre at Curtin University and Shaomin Liu at Curtin University for DSC-TGA equipment access. The authors would like to acknowledge Drew A. Sheppard for insightful discussions.

Notes and references

1. U. Heyder, S. Schaphoff, D. Gerten and W. Lucht, *Environmental Research Letters*, 2011, **6**, 034036.
2. X. Py, Y. Azoumah and R. Olives, *Renewable and Sustainable Energy Reviews*, 2013, **18**, 306-315.
3. S. Kuravi, J. Trahan, D. Y. Goswami, M. M. Rahman and E. K. Stefanakos, *Progress in Energy and Combustion Science*, 2013, **39**, 285-319.
4. T. Bauer, N. Pfleger, N. Breidenbach, M. Eck, D. Laing and S. Kaesche, *Applied Energy*, 2013, **111**, 1114-1119.
5. S. Kraemer, Crescent Dunes 24-Hour Solar Tower Is Online, https://cleantechnica.com/2016/02/22/crescent-dunes-24-hour-solar-tower-online, (accessed January 24, 2019).
6. P. Pardo, A. Deydier, Z. Anxionnaz-Minvielle, S. Rougé, M. Cabassud and P. Cognet, *Renewable and Sustainable Energy Reviews*, 2014, **32**, 591-610.
7. D. A. Sheppard, M. Paskevicius, T. D. Humphries, M. Felderhoff, G. Capurso, J. Bellosta von Colbe, M. Dornheim, T. Klassen, P. A. Ward, J. A. Teprovich, C. Corgnale, R. Zidan, D. M. Grant and C. E. Buckley, *Applied Physics A*, 2016, **122**, 395.
8. G. G. Libowitz, *US Pat.,* 4040410 (1977)
9. M. Paskevicius, D. A. Sheppard and C. E. Buckley, *Journal of the American Chemical Society*, 2010, **132**, 5077-5083.
10. K. Manickam, P. Mistry, G. Walker, D. Grant, C. E. Buckley, T. D. Humphries, M. Paskevicius, T. Jensen, R. Albert, K. Peinecke and M. Felderhoff, *Int. J. Hydrogen Energy*, 2019, DOI: https://doi.org/10.1016/j.ijhydene.2018.12.011.
11. D. N. Harries, M. Paskevicius, D. Sheppard, T. Edward Cameron Price and C. E. Buckley, *Proceedings of the IEEE*, 2012, **100**, 539-549.
12. M. Fellet, C. E. Buckley, M. Paskevicius and D. A. Sheppard, *MRS Bulletin*, 2013, **38**, 1012-1013.

13. C. Corgnale, B. Hardy, T. Motyka, R. Zidan, J. A. Teprovich and B. Peters, *Renewable and Sustainable Energy Reviews*, 2014, **38**, 821-833.
14. T. D. Humphries, D. A. Sheppard, M. R. Rowles, M. V. Sofianos and C. E. Buckley, *Journal of Materials Chemistry A*, 2016, **4**, 12170-12178.
15. M. S. Tortoza, T. D. Humphries, D. A. Sheppard, M. Paskevicius, M. R. Rowles, M. V. Sofianos, K. F. Aguey-Zinsou and C. E. Buckley, *Phys Chem Chem Phys*, 2018, **20**, 2274-2283.
16. D. A. Sheppard, C. Corgnale, B. Hardy, T. Motyka, R. Zidan, M. Paskevicius and C. E. Buckley, *RSC Advances*, 2014, **4**, 26552-26562.
17. C. Wolverton and V. Ozoliņš, *Physical Review B*, 2007, **75**, 064101.
18. T. Motyka and Z. Zidan, *Low-Cost Metal Hydride Thermal Energy Storage System for Concentrating Solar Power Systems*, Report SRNL-STI-2017-00017, sti.srs.gov, 2016.
19. J.-C. Crivello, B. Dam, R. V. Denys, M. Dornheim, D. M. Grant, J. Huot, T. R. Jensen, P. de Jongh, M. Latroche, C. Milanese, D. Milčius, G. S. Walker, C. J. Webb, C. Zlotea and V. A. Yartys, *Applied Physics A*, 2016, **122**, 97.
20. M. P. Pitt, M. Paskevicius, C. J. Webb, D. A. Sheppard, C. E. Buckley and E. M. Gray, *International Journal of Hydrogen Energy*, 2012, **37**, 4227-4237.
21. D. A. Sheppard, T. D. Humphries and C. E. Buckley, *Applied Physics A*, 2016, **122**, 406.
22. A. Bouamrane, C. de Brauer, J. P. Soulié, J. M. Létoffé and J. P. Bastide, *Thermochimica Acta*, 1999, **326**, 37-41.
23. A. Bouamrane, J. P. Laval, J. P. Soulie and J. P. Bastide, *Materials Research Bulletin*, 2000, **35**, 545-549.
24. K. Ikeda, Y. Kogure, Y. Nakamori and S. Orimo, *Scripta Materialia*, 2005, **53**, 319-322.
25. D. A. Sheppard, M. Paskevicius and C. E. Buckley, *Chemistry of Materials*, 2011, **23**, 4298-4300.
26. S. Tao, Z. Wang, Z. Wan, J. Deng, H. Zhou and Q. Yao, *International Journal of Hydrogen Energy*, 2017, **42**, 3716-3722.
27. Z. Wang, S. Tao, J. Deng, H. Zhou and Q. Yao, *International Journal of Hydrogen Energy*, 2017, **42**, 8554-8559.
28. Z. Wang, S. Tao, J. Li, J. Deng, H. Zhou and Q. Yao, *Metals*, 2017, **7**, 9.
29. P. A. Ward, C. Corgnale, J. A. Teprovich, T. Motyka, B. Hardy, B. Peters and R. Zidan, *Journal of Alloys and Compounds*, 2015, **645**, S374-S378.
30. F. S. Yang, G. X. Wang, Z. X. Zhang, X. Y. Meng and V. Rudolph, *International Journal of Hydrogen Energy*, 2010, **35**, 3832-3840.
31. K. Jiao, X. Li, Y. Yin, Y. Zhou, S. Yu and Q. Du, *Applied Energy*, 2012, **94**, 257-269.
32. M. Botzung, S. Chaudourne, O. Gillia, C. Perret, M. Latroche, A. Percheronguegan and P. Marty, *International Journal of Hydrogen Energy*, 2008, **33**, 98-104.
33. C. A. Chung, S. W. Yang, C. Y. Yang, C. W. Hsu and P. Y. Chiu, *Applied Energy*, 2013, **103**, 581-587.
34. M. Gambini, M. Manno and M. Vellini, *International Journal of Hydrogen Energy*, 2008, **33**, 6178-6187.
35. M. Raju and S. Kumar, *International Journal of Hydrogen Energy*, 2012, **37**, 2767-2778.
36. M. Paskevicius, D. A. Sheppard, K. Williamson and C. E. Buckley, *Energy*, 2015, **88**, 469-477.
37. D. Dong, T. D. Humphries, D. A. Sheppard, B. Stansby, M. Paskevicius, M. V. Sofianos, A. L. Chaudhary, M. Dornheim and C. E. Buckley, *Sustainable Energy & Fuels*, 2017, **1**, 1820-1829.
38. M. D. Mat, Y. Kaplan and K. Aldas, *International Journal of Energy Research*, 2002, **26**, 973-986.
39. L. Popilevsky, V. M. Skripnyuk, Y. Arnouyal and E. Rabkin, *International Journal of Hydrogen Energy*, 2017, **42**, 22395-22405.
40. A. Chaise, P. de Rango, P. Marty, D. Fruchart, S. Miraglia, R. Olivès and S. Garrier, *International Journal of Hydrogen Energy*, 2009, **34**, 8589-8596.
41. C. Pohlmann, L. Röntzsch, S. Kalinichenka, T. Hutsch and B. Kieback, *International Journal of Hydrogen Energy*, 2010, **35**, 12829-12836.
42. R. Urbanczyk, M. Meggouh, R. Moury, K. Peinecke, S. Peil and M. Felderhoff, *Applied Physics A*, 2016, **122**, 315.
43. M. Paskevicius, D. A. Sheppard and C. E. Buckley, *Journal of the American Chemical Society*, 2010, **132**, 5077-5083.
44. B. Satya Sekhar, M. Lototskyy, A. Kolesnikov, M. L. Moropeng, B. P. Tarasov and B. G. Pollet, *Journal of Alloys and Compounds*, 2015, **645**, S89-S95.
45. K. Komiya, N. Morisaku, R. Rong, Y. Takahashi, Y. Shinzato, H. Yukawa and M. Morinaga, *Journal of Alloys and Compounds*, 2008, **453**, 157-160.
46. D. Pottmaier, E. R. Pinatel, J. G. Vitillo, S. Garroni, M. Orlova, M. Baró, G. B. M. Vaughan, M. Fichtner, W. Lohstroh and M. Baricco, *Chemistry of Materials*, 2011, **23**, 2317-2326.
47. K. Ikeda, S. Kato, Y. Shinzato, N. Okuda, Y. Nakamori, A. Kitano, H. Yukawa, M. Morinaga and S. Orimo, *Journal of Alloys and Compounds*, 2007, **446**, 162-165.
48. F. D. Manchester and A. S. M. International, *Phase diagrams of binary hydrogen alloys*, ASM International, Materials Park, OH, 2000.
49. Z. Bao, F. Yang, Z. Wu, X. Cao and Z. Zhang, *Applied Energy*, 2013, **112**, 1181-1189.
50. J.-H. Shim, M. Park, Y. H. Lee, S. Kim, Y. H. Im, J.-Y. Suh and Y. W. Cho, *International Journal of Hydrogen Energy*, 2014, **39**, 349-355.
51. E. W. Lemmon, M. L. Huber and M. O. McLinden, *NIST Standard Reference Database 23*, 2013.